Performance of intrinsic heteroatoms in CoP@ginkgo leave-based carbon material on promoting the electrocatalytic activity during HER and OER

Qichang Wang[a], Ran Yu[a], Dekui Shen[a*], Kai Hong Luo[b], Chunfei Wu[c], Sai Gu[d]

[a] Key Laboratory of Energy Thermal Conversion and Control of Ministry of Education, School of Energy and Environment, Southeast University, Nanjing 210096, Jiangsu, PR China

[b] Department of Mechanical Engineering, University College London, London, WC1E 7JE, United Kingdom

[c] School of Chemistry and Chemical Engineering, Queen's University Belfast, Belfast, BT7 1NN, United Kingdom

[d] Faculty of Engineering and Physical Sciences, University of Surrey, Guilford, GU2 7XH, United Kingdom

* Corresponding author: * 101011398@seu.edu.cn (D. K. Shen)

Abstract: Nitrogen (N) and sulfur (S) in ginkgo leaves were converted to carbon lattice heteroatoms, making them a matrix. Herein, cobalt phosphide (CoP) was loaded on the N/S/phosphorus (P) co-doped carbon matrix (CoP@NSPC) via the carbothermic reduction method using the ginkgo leave-based carbon as the precursor. A N/P co-doped carbon matrix (CoP@NPC) was also prepared using glucose-based carbon as the support. Effects of intrinsic heteroatoms from ginkgo leaves were revealed through XPS and UPS compared with CoP@NPC. The N/S heteroatoms accelerated the electron transfer and adjusted the d-band center of CoP@NSPC, thus causing a faster

electrocatalytic process. The as-obtained CoP@NSPC exhibited excellent activity toward HER (160 mV @ 10 mA cm^{-2}) and OER (198 mV @ 10 mA cm^{-2}). The assembly feasibility and catalytic performance were further verified in overall water splitting and exhibited high efficiency and long durability of CoP@NSPC.

Key words: ginkgo leaves, N/S/P co-doped carbon, CoP, d-band, water splitting

1 Introduction

Hydrogen gas (H_2) is an environment-friendly and carbon-neutral energy carrier that may be a prospective alternative to traditional fossil fuels [1-4]. The current industrial H_2 production was based on steam reforming, which consumes renewable fossil fuels and causes the emission of greenhouse gases [5, 6]. By comparison, electrocatalytic overall water splitting assembled with renewable energy has been regarded as a sustainable route for H_2 generation [7, 8]. However, limited to the high cost, rare natural abundance and inferior stability of precious metal-based catalysts, electrocatalytic H_2 production through water electrolysis still can not meet the requirements of large-scale application. Hence, many research efforts are devoted to searching the affordable and highly active alternatives of noble-metal catalysts [1, 9-12]. The transition metal (TM)-based catalysts such as carbides, sulfides, phosphides, etc., have been widely explored [1, 13-15]. In particular, the transition metal phosphides (TMPs) have drawn much attention, where cobalt phosphide (CoP) was regarded as one of the appealing candidates of noble metal-based catalysts for both hydrogen evolution reaction (HER) and oxygen evolution reaction (OER). The phosphorus (P) atoms with high

electronegatively in CoP were proved to be the proton acceptor and draw electrons from metal, thus accelerating the electron transfer and enhancing the electrocatalytic activity [16-18].

However, the easy agglomeration and unsuitable adsorption/desorption energy with intermediates (eg. HO^*, H^*, etc.) of CoP during the HER and OER process seriously restricted its utilisation [19, 20]. Loading CoP on the carbon matrix is a feasible method to protect the nanoparticles from agglomeration and optimise the binding energy with intermediates [20, 21]. Furthermore, the introduction of foreign atoms into the carbon lattice will further adjust the electronic structure and energy level of CoP supported carbon catalysts, which will lead to moderate binding energy (BE) with various intermediates in both HER and OER processes [22, 23]. Biomass is an attractive carbon precursor. Its nitrogen (N) and sulfur (S) containing organic components could be directly introduced into the carbon skeleton with a simple pyrolysis process [24-28], thus endowing biomass-based carbon with a possibility to be the support for CoP. It is noted that larger amounts of biomass waste were produced every year, while most of them were burned or buried, even causing secondary pollution. In order to take full use of the advantages of biomass, the intrinsic dopants of biomass-based carbon promoting the electrocatalytic activity of CoP are interesting but lack in-depth study. Particularly, the role of the dopants in the biomass-based carbon on the band structure and electronic properties of CoP deserves detailed analysis.

The position of d-band centers is related to the binding energy of intermediates in the electrochemistry process, which is critical for electrocatalytic activities. While the dopants in carbon lattice reconstruct the d-band structure of CoP, the effect of dopants from biomass on the d-band center of CoP is not clear. Therefore, in this work, ginkgo leaves were used as the carbon sources to prepare the N/S doped carbon, which was then loaded with CoP. The non-dopant carbon was obtained from glucose without any N/S element widely existing in the ginkgo leaves [29]. The d-band center of such two samples was investigated to analyse the role of N/S atoms from ginkgo leaves. Moreover, the relationship between N/S atoms with high electronegatively in the carbon lattice with the electron transfer was revealed.

2 Experiment section

2.1 Materials

Cobalt (II) nitrate hexahydrate ($Co(NO_3)_2 \cdot 6H_2O$, 99.99%), Zinc chloride ($ZnCl_2 \cdot 6H_2O$, 99.99%), Magnesium chloride ($MgCl_2 \cdot 6H_2O$, 99.99%), 2-methylimidazole (2-MeMI), glucose, phytic acid (PA, 55~70 wt.%) were purchased from Sinopharm Chemical Reagent Co., Ltd. and used without purification. The ginkgo leaves were collected in Nanjing, Jiangsu Province, China, were washed with ultrapure water several times to remove the dirt. The clean ginkgo leaves were dried for a whole night in an oven at 80 ^{o}C and then crushed to obtain the ginkgo leave powders.

2.2 Preparation of NSC and CoP@NSPC

The $ZnCl_2 \cdot 6H_2O$ (1 g) and $MgCl_2 \cdot 6H_2O$ (2 g) was used as the activation agent and template to grind with the ginkgo leave powders (1 g) for 20 mins and pyrolysis at 750 ^oC for 2 h with the protection of N_2; the as-obtained carbon was named nitrogen and sulfur co-doped carbon (NSC).

The CoP@NSPC was prepared via the carbothermal reduction method using the NSC as the carbon source and support. Firstly, 120 mg NSC was dispersed in 10 mL ultrapure water to form homogenous suspension A. The 30 mg $Co(NO_3)_2 \cdot 6H_2O$ and 42 mg 2-MeMI were dissolved in 5 mL ultrapure water, respectively. Then, the two solutions were mixed and stirred for 30 mins to obtain blue suspension B. The 250 μL PA was injected into the suspension B and subsequently, suspension A was added to suspension B. The mixed suspension was vigorously stirred for 6 h and evaporated moisture via water bath at 60 ^oC, then dried at 80 ^oC in a vacuum. The dry powder was transferred into the tube furnace and calcined at 900 ^oC for 2 h in an N_2 atmosphere. The as-prepared black powders were named CoP@NSPC.

2.3 Preparation of non-dopants carbon and CoP@NPC

The non-dopants carbon and CoP@NPC were prepared via the same procedure as NSC and CoP@NSPC, except the ginkgo leaves powders was replaced by glucose.

2.4 Material characterisations

The morphology of the as-obtained catalysts was revealed via scanning electron

microscopy (SEM, FEI quanta 400FEG), transmission electron microscopy (TEM, FEI Tecnai 20 electron microscope) and the high-angle annular dark field-scanning transmission electron microscope (HAADF-STEM, FEI TALOSF200S). The X-ray powder diffraction (XRD, Bruker D8) was employed to study the structural compositions and valence state of the catalysts. The specific surface area was analysed via the N_2 adsorption experiment on the Quanta 250F and FEI by Brunauer-Emmett Teller (BET). To further investigate the element dispersion and chemical states on the materials surface, the K-Alpha X-ray photoelectron spectroscopy (XPS) was taken on Thermo ESCALAB 250XI, and calibrated with the binding energy using C1s at 284.6 eV. The Raman spectra were conducted using iHR550 Raman microscope (HOR-IBA scientific) at a range of 400~4000 cm^{-1}. The ultraviolet electron spectroscopy (UPS, Phi5000 VersaProbeIII) was taken to obtain the valence band spectrum of materials. Furthermore, the work function spectrum was measured via UPS with a bias voltage of -10 V.

2.5 Electrochemical measurement

Electrocatalytic measurements for HER and OER were conducted in 0.5 M H_2SO_4 and 1 M KOH using a conventional three-electrode system on CHI 760E electrochemical workstation at room temperature with N_2 and O_2 saturation, respectively. The graphite rod was selected as the counter electrode. The mercury/mercurous sulfate electrode (Hg/Hg_2SO_4) and mercury/mercuric oxide electrode (Hg/HgO) was used as the reference electrode in 0.5 M H_2SO_4 and 1 M KOH, respectively. The glass carbon

electrode (GCE, 0.196 cm^{-2}) was served as the working electrode with the modification of the catalysts ink. Such catalysts ink was prepared by mixing the 10 mg of the as-obtained catalysts with 1000 μL of ethanol/deionised water ($V_{C_2H_5OH} : V_{H_2O} = 1 : 3$) and sonicated for 30 minutes. The well-mixed catalysts ink of 10 μL was dropped onto the GC and dried at 25 ºC. Subsequently, the 10 μL Nafion (5 wt.%) was dropped onto the GC and dried naturally. The linear sweep voltammetry (LSV) plots were recorded with a scan rate of 2 mV s^{-1}. Cyclic voltammetry (CV) tests for HER and OER were performed at a range of -0.5~-0.3 V and -0.2~0 eV, respectively, with a scan rate of 10, 30, 50, 70, 90 mV s^{-1}, respectively. The overall water splitting was performed with a H-cell. Moreover, all the HER and OER tests were taken with IR-correct and the measured potentials were converted to a reversible hydrogen electrode (RHE) using Eq.(a) and Eq.(b), respectively.

$$E_{vs.RHE} = E_{vsHg/Hg_2SO_4} + E^{\theta}_{Hg/Hg_2SO_4} + 0.059\ pH \qquad (a)$$

$$E_{vs.RHE} = E_{vsHg/HgO} + E^{\theta}_{Hg/HgO} + 0.059\ pH \qquad (b)$$

Where, E^{θ}_{Hg/Hg_2SO_4} was equal to 0.697 V and $E^{\theta}_{Hg/HgO}$ was equal to 0.098 V.

3 Results and discussion

3.1 Physical-chemistry properties

The mass ratio of $Co(NO_3)_2 \cdot 6H_2O$ and NSC was first explored for optimal preparation. As shown in Figure S1, the HER and OER tests were conducted to prove the best mass ratio of $Co(NO_3)_2 \cdot 6H_2O$ and NSC was 1:4. Then, compared with samples prepared via non-dopants carbon skeleton derived from glucose, the role of inherent N/S atoms in

ginkgo leaves was further revealed. CoP@NSPC and CoP@NPC were prepared via the same steps as shown in scheme 1; thus, the effects of nitrogen atoms introduced by 2-MeMI is considered to be identical here.

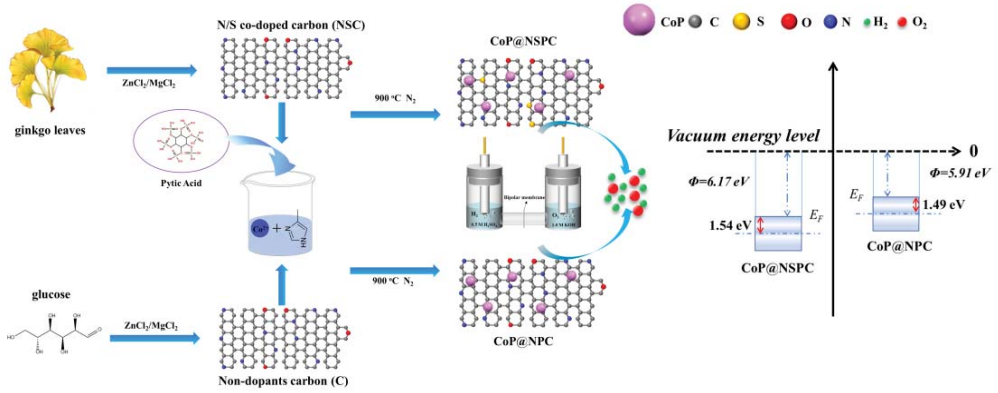

Scheme 1. Synthesis process CoP@NSPC and CoP@NPC

The morphology and structures of CoP@NSPC and CoP@NPC were investigated through SEM. Benefiting from the activation of $MgCl_2$ and $ZnCl_2$, there are abundant pores on the surface of CoP@NSPC (Figure 1a) and CoP@NPC (Figure S2). The porous structure of CoP@NSPC and CoP@NPC mainly consists of microporous and mesoporous, which may meet the demands of fast mass transfer [1] and promote the exposure of active sites inside of the materials [30]. The HAADF-STEM was employed to explore further the dispersion of CoP nanoparticles (NPs) in CoP@NSPC. As shown in Figure 1b, the highly dispersed light flake particles in the dark field image are the CoP NPs with an average size of 25.26 nm (Figure S3). The fringe spacing with 2.79 Å corresponds to the (002) lattice planes of CoP.

Moreover, the EDS elemental mapping shown in Figure 1e confirms that the elementals including C, N, O, S, P are distributed over the entire as-obtained materials, while the

Co is mainly dispersed as the nanoparticles in the form of CoP. Meanwhile, due to the unavoidable surface oxidation upon exposure to air, the appearance of slightly oxidised P and Co states can be usually observed in CoP@NSPC. The S element exists mainly in the form of doping. The detailed analysis is discussed in the XRD and XPS sections.

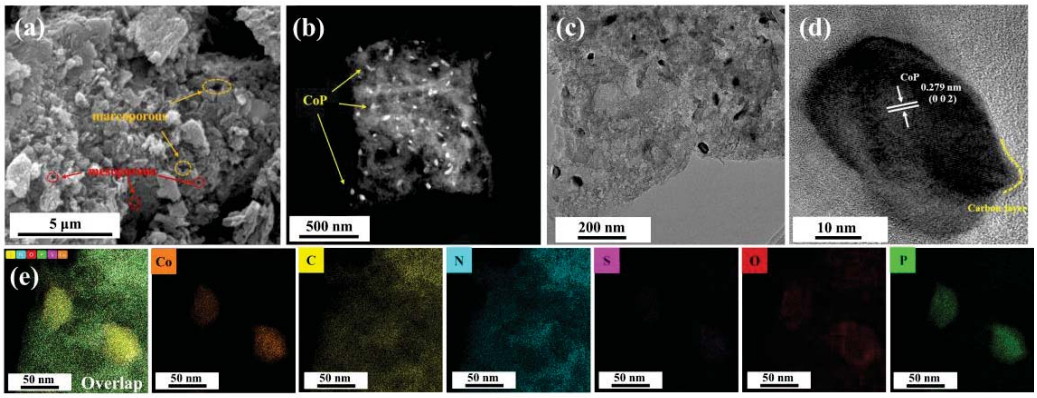

Figure 1. (a) SEM, (b) HAADF-STEM, (c, d) HRTEM images and (e) EDS elemental mapping images of CoP@NSPC.

As shown in Figure 2a, the XRD patterns further confirm the successful preparation of CoP NPs loaded on the N/P/S co-doped carbon support, which was consistent with the HAADF-STEM results. It is evident that the diffraction peak positions of CoP@NSPC and CoP@NPC are the same. The broad peak at the 26° represents the (0 0 2) lattice plane of graphite carbon [21]. The diffraction peaks at 32 °, 36 °, 46 °, 48 °, 52 °, and 57 ° are indexed to the (011), (002), (200), (111), (102), (210), (112), (211), (103), (020) and (212) planes of CoP according to the JCPDS-29-0497. In addition, the pore structure of CoP@NSPC and CoP@NPC was studied by N_2 adsorption and desorption experiments. The adsorption isotherm (Figure 2b) corresponds to the type IV isotherms,

which means the hole of CoP@NSPC and CoP@NPC mainly consists of mesoporous [31]. The pore size distribution shown in Figure S4 has further confirmed the existence of mesoporous and macroporous. Such hierarchical porous structure endows the CoP@NSPC and CoP@NPC with a high specific surface area of 733.99 m^2/g and 1069 m^2/g, respectively. Since the CoP@NSPC and CoP@NPC owned similar crystal structure and pore structure, the key role to result in the different performance on HER and OER for CoP@NSPC and CoP@NPC needs in-depth discussion through Raman and XPS spectrum.

There are two distinct peaks in the Raman spectrum (Figure 2c), the peak at 1350 cm^{-1} and 1580 cm^{-1} named D and G band, representing the disordered carbon and graphite carbon, respectively. The ratio of the intensity of the D band and G band indicated the number of defects in the carbon support. At the same time, the I_D/I_G for CoP@NSPC is 1.05, greater than that of CoP@NPC (1.00). Hence, such results implied the CoP@NSPC with more defects, which can be further confirmed by the XPS spectrum. As shown in Table S1, there are more N/S contents in the CoP@NSPC compared with CoP@NPC. Considering the N atoms introduced by 2-MeMI is roughly equal, the difference of the N atoms is mainly caused by the pristine heteroatoms derived from ginkgo leaves. The N, S, O, P was proved to be doped in the carbon skeleton of CoP@NSPC, which is consistent with the element mapping image. The high-resolution N 1s spectrum of CoP@NSPC can be subdivided into four peaks at 400.8, 398.45, 402.08 eV, and 399.78 eV (Figure 2d) represents the pyrrolic N, pyridinic N, graphitic

N and Co-N, respectively. By taking advantage of the rich amount of N containing organic contents in ginkgo leaves, the atoms ratio of pyrrolic N, pyridinic N, graphitic N and Co-N were both higher than CoP@NPC as shown in Table S2, which will offer more active sites and accelerate the diffusion-limited current density [30]. The high-resolution S 2p spectrum of CoP@NSPC can be deconvoluted into three peaks, while there are no S elements in the CoP@NPC as shown in Figure 2g (Table S3). The three peaks located on the 163.79 eV, 164.89 eV and 169.19 eV correspond to the presence of S-C-S, C=S and C-SO_x-C, respectively [32]. There are four distinct peaks at 798.09 eV, 781.93 eV, 803.58 eV and 786.99 eV in the high-resolution Co 2p spectrum, namely Co $2p_{1/2}$, Co $2p_{3/2}$ and Co oxidations states [20-22, 33]. Compared with CoP@NPC, the content of Co is increased, which may result from the promotion of Co-anchoring on the carbon skeleton induced by the presence of more electronegative atoms doping [34]. Notably, compared with CoP@NPC, the BE of Co-N for N 1s of CoP@NSPC was a negative shift, while the BE of Co-N for Co 2p was a positive shift (Table S4). The plentiful N atoms significantly enhance the electron transfer for CoP@NSPC, which may adjust the electronic structure and accelerate the electrocatalysis process [22, 35]. The high-resolution O 1s spectrum of CoP@NSPC and CoP@NPC can be deconvoluted into three peaks at 530.86, 532.13 and 533.18, as shown in Figure S6, corresponding to the O-Co, O-C and O-P. As shown in Figure 2h, the chemical states of P were basically the same, which are four distinct peaks located at 134.36, 132.98, 130.15 and 129.71 in the high-resolution P 2p spectrum, corresponding to the P-O, P-C, P $2p_{1/2}$ and P $2p_{2/3}$.

Furthermore, the dopants could reconstruct the electronic structure of CoP, which may affect the adsorption and desorption energy of various intermediates [36]. The d-band center is the descriptor of the free energy of hydrogen (oxygen) adsorption. To uncover the d-band center of CoP@NSPC and CoP@NPC, the UPS valence band spectra was employed to calculate the work function and the location of the d-band center. Shown in Figure S7 is the work function spectrum derived from the UPS valance band spectrum with a -10 V bias. Since the secondary electron cut-off edges for CoP@NSPC and CoP@NPC are 15.05 eV and 15.31 eV, the values of work function (Φ) for CoP@NSPC and CoP@NPC are 6.17 eV and 5.91 eV, respectively. The higher work function value indicates the Fermi level for CoP@NSPC shifts away from vacuum level compared with CoP@NPC and its d-band shifts away from the vacuum level. Through the raw UPS valence band spectrum (Figure S8), the d-band center can be obtained from the linear intersection near the Fermi level, as shown in Figure 2e [37]. The d-band centers for CoP@NSPC and CoP@NPC are 1.54 eV and 1.49 eV respectively. The downshift of the d-band center optimises the adsorption/desorption energy with intermediates of HER and OER, which is beneficial to the electrocatalytic activity of CoP@NSPC.

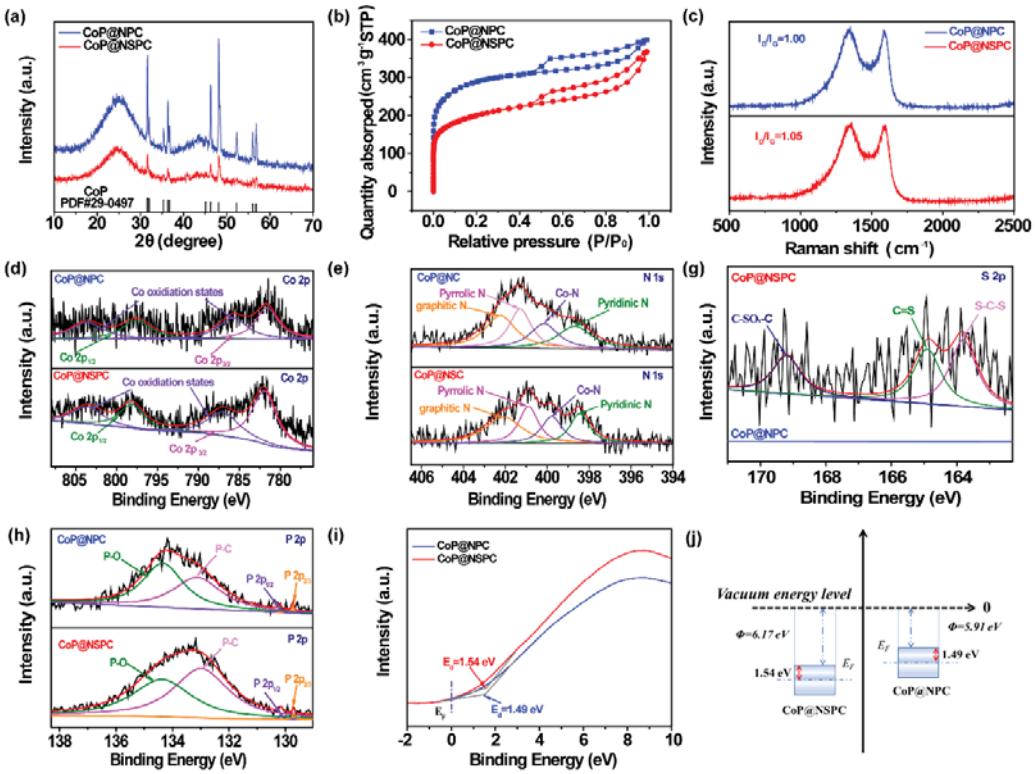

Figure 2. (a) XRD patterns, (b) N_2 sorption isotherms, and (c) Raman spectrum of CoP@NSPC and CoP@NPC, High resolution XPS spectrum of (d) N 1s, (e) S 2p, (f) Co 2p and (g) P 2p of CoP@NSPC and CoP@NPC, (h) UPS valence band spectra of CoP@NSPC and CoP@NPC, (i) schematic of energy band structure.

3.2 Electrocatalytic activity and stability towards HER

The HER activity for CoP@NSPC, CoP@NPC and 20% Pt/C were assessed through the linear scan voltammogram (LSV) polarisation curves recorded in 0.5 M H_2SO_4. Shown in Figure 3a was the IR-compensated LSV curves. The CoP@NSPC manifests outstanding HER performances while the CoP@NPC has poor HER activity. To obtain 10 and 50 mA cm^{-2} current density, the designed CoP@NSPC delivers a low overpotential of 160 and 256 mV, as shown in Figure 3a, much smaller than CoP@NPC

(214 and 331 mV). The HER reaction kinetics of CoP@NSPC and CoP@NPC was then determined via Tafel diagrams. As shown in Figure 3b, CoP@NSPC demonstrates a lower Tafel slope of 87.3 mV dec^{-1} than CoP@NPC, indicating better HER catalytic activity. The Tafel slopes for CoP@NSPC do not match the ideal Tafel slopes of 29, 38 and 116 mV dec^{-1} corresponding to different rate-determining steps of HER, suggesting the HER proceeds CoP@NSPC via a Volmer–Heyrovsky mechanism [21]. The electrochemical impedance spectroscopy (EIS) test was employed to evaluate the charge transfer resistance (R_{ct}) of the as-prepared catalyst [38]. The Nyquist plots in Figure S9a for CoP@NSPC have shown a smaller semicircle which indicated the lower value of R_{ct}, revealing the higher conductivity and faster electron transfer of CoP@NSPC compared with CoP@NPC, which is consistent with XPS results. The efficient catalytic surface area (ECSA) was calculated to further understand the superb catalytic activity of CoP@NSPC [17]. The double-layer capacitor (C_{dl}) associated with ECSA arose from cyclic voltammetry (CV) with different scan rates, as shown in Figure S10. As shown in Figure 3c, the fitted C_{dl} of CoP@NSPC is 109.4 mF cm^{-2}, higher than CoP@NPC (98.2 mF cm^{-2}), suggesting there are more accessible active sites in CoP@NSPC. Besides, the stability of catalytic activity is also critical for its practical application. The chronoamperometric response (i-t) was performed under the current density of 10 mA cm^{-2} to access the stability of CoP@NSPC. After 8 h operation, it has shown a 97.8% current density retention (Figure 3d), which means the robust catalytic activity of CoP@NSPC. The internal diagram is the LSV curves before and after 5000 CV cycles. The overpotential to drive the current density to 10 mA cm^{-2} was with a

negligible increase of ~4 mV.

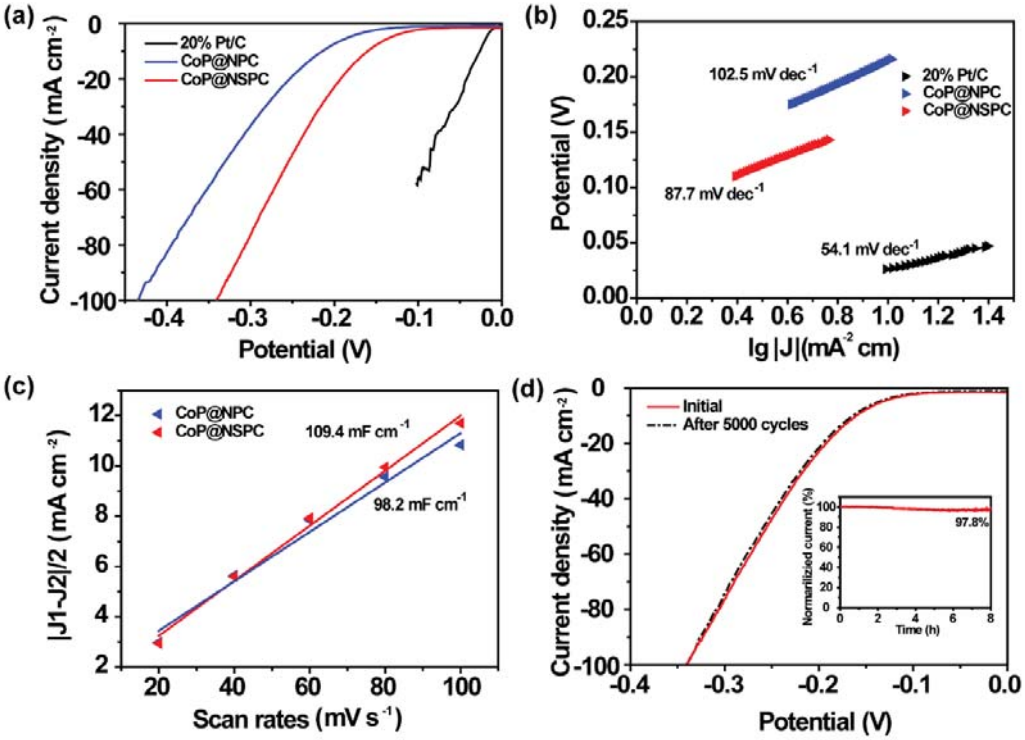

Figure 3. Electrocatalytic HER performance. (a) LSV curves and (b) Corresponding Tafel plots in 0.5 M H_2SO_4, (c) C_{dl} stands for ECSA for CoP@NSPC and CoP@NPC, (d) Durability test of CoP@NSPC.

3.3 Electrocatalytic activity and stability towards OER

The OER performance of CoP@NSPC, CoP@NPC and commercial IrO_2 was also investigated via a standard three-electrolyte system in 1.0 M KOH. The LSV curves in Figure 4a demonstrate that CoP@NSPC exhibit superb OER activity, in which only 198 and 345 mV overpotential is required to deliver 10 mA cm^{-2} current density, comparable to the commercial IrO_2 (173 and 339 mV). To reveal the reaction kinetics of OER activity, the Tafel plots are obtained corresponded to the LSV plots, as shown in Figure

4b. The smaller Tafel plots of CoP@NSPC (179.1 mV dec^{-1}) suggested better scaling kinetics with voltage [39-41], which means faster kinetics and optimised OER activity. Such a faster OER process was also proved by EIS testing. The semicircle of CoP@NSPC with a smaller radius demonstrates the stronger charge transfer among the OER process (Figure S9b). The C_{dl} for OER was also investigated based on CV curves on different scan rates (Figure S11). As shown in Figure 4c, it is no doubt that the value of C_{dl} for CoP@NSPC (54.9 mF cm^{-2}) is higher, which indicate it is favorable to expose more active sites compared with CoP@NPC (48.2 mF cm^{-2}). Similar to the HER process, the long-term stability was conducted via i-t testing at 10 mA cm^{-2}. The CoP@NSPC performed robust durability with a mild density attenuation (~9.6%). Furthermore, the stability evaluation is also performed by comparing the LSV curves before and after 5000 CV cycles. As shown in the internal diagram of Figure 4d, the overpotential to deliver 10 mA cm^{-2} current density exhibits a slight increase of 25 mV, confirming the outstanding stability of CoP@NSPC for OER.

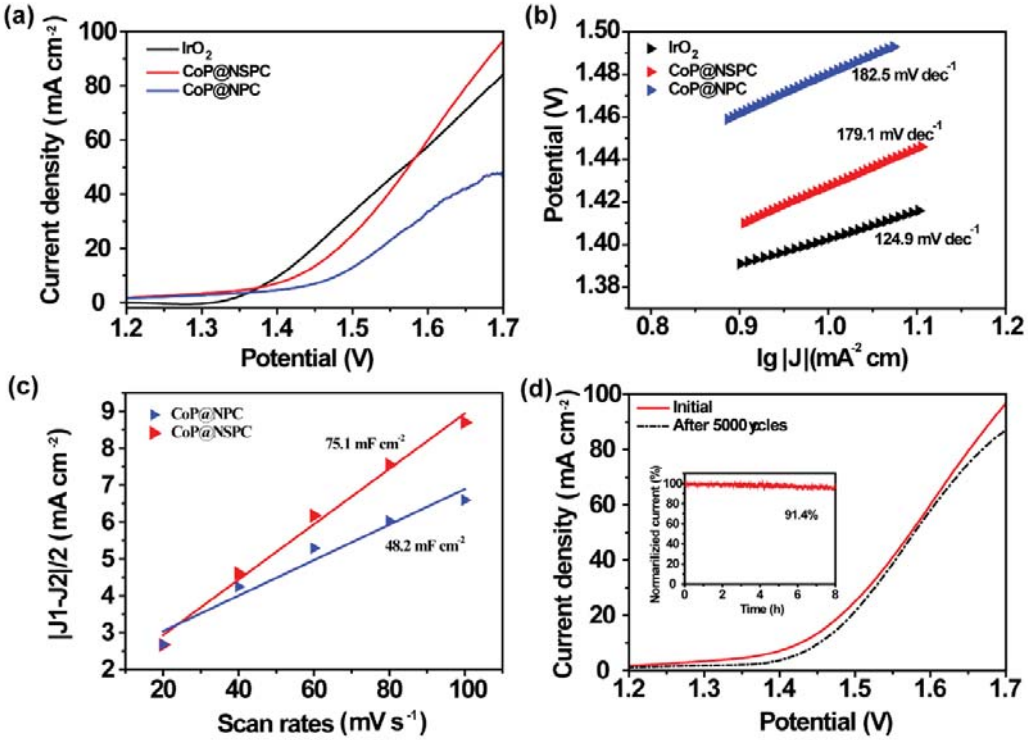

Figure 4. Electrocatalytic OER performance. (a) LSV curves and (b) Corresponding Tafel plots in 1.0 M KOH, (c) C_{dl} stands for ECSA for CoP@NSPC and CoP@NPC, (d) Durability test of CoP@NSPC.

The observation of the superior HER and OER activity of the CoP@NSPC compared with CoP@NPC was mainly attributed to the following three reasons. First, the adsorption energy of CoP with H_2 and O_2 was too strong, which will limit the process of H_2/O_2 desorption. The carbon matrix with rich N/S dopants resulted in the downshift of the d-band center, which optimised the adsorption/desorption with H_2/O_2, thus causing a faster HER and OER process for CoP@NSPC. The dopants of N/S atoms also can serve as the additional active sites, which was in accordance with the higher value of C_{dl} of CoP@NSPC. More than that, the dopants accelerated the electron

transfer between Co sites to the carbon matrix. The fine XPS spectrum of N species of CoP@NSPC have shown a negative shift. In contrast, the peaks of Co species was positively shifted compared with CoP@NPC, indicating there was favorable charge transfer during the electrocatalytic process. Such results were further proved via EIS tests for that the CoP@NSPC had a smaller impedance.

3.4 Electrocatalytic activity and stability towards overall water splitting

The overall water splitting was performed with a two-electrode device in H-type cell, while the anode and cathode were assembled with the bifunctional electrocatalysts of CoP@NSPC. The HER and OER process was conducted in 0.5 M H_2SO_4 and 1.0 M KOH, respectively. The ion exchange membrane was used to exchange the ions of these two electrolytes. As shown in Figure 5a, the CoP@NSPC || CoP@NSPC only needed a cell voltage of 1.13 and 1.38 V to deliver the current density to 10 and 50 mA cm^{-2}, which was comparable to commercial IrO_2 || Pt/C. With the increase of the cell voltage, the current density of CoP@NSPC || CoP@NSPC even exceeds the commercial IrO_2 || Pt/C. Figure 5b shows the durability test of CoP@NSPC || CoP@NSPC for water splitting. After 10 h operation at the current density of 10 mA cm^{-2}, there was only a slight current density attenuation of 8.8%, suggesting the excellent robustness for overall water splitting.

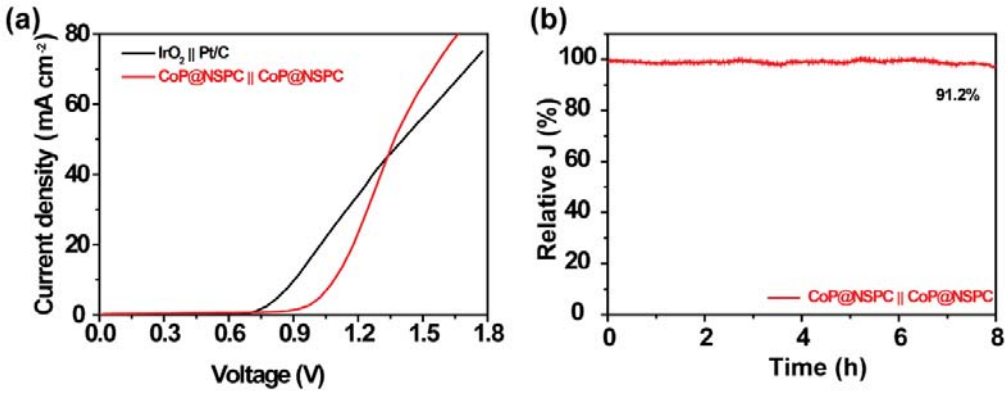

Figure 5. Overall water splitting performance. (a) Polarization curves of IrO_2 || Pt/C and CoP@NSPC || CoP@NSPC, (b) Stability of CoP@NSPC || CoP@NSPC.

4 Conclusion

The as-prepared CoP@NSPC was fabricated using ginkgo leaves derived carbon via a facile carbothermic reduction strategy. The hybrid catalysts exhibit bifunctional catalytic activity toward the HER and OER processes. Owing to the intrinsic N/S atoms doping in the ginkgo leaves derived carbon, CoP@NSPC shows better catalytic activity for HER and OER compared with CoP@NPC. The heteroatoms in the carbon matrix of CoP@NSPC have been shown to induce faster electron transfer between Co NPs and carbon matrix. The d-band center of CoP@NSPC moves downwards, resulting in moderate adsorption and desorption of intermediates in the HER and OER processes. CoP@NSPC acted as both anode and cathode in the H-type cell, achieving a current density of 10 and 50 mA cm^{-2} at 1.13 and 1.38 V, together with excellent stability.

Declaration of competing interest

The authors declare that they have no known competing financial interests or personal

relationships that could have appeared to influence the work reported in this paper.

Acknowledgements

The authors gratefully acknowledge the support of National Natural Science Foundation (51878145 and 51861145102), and Jiangsu Provincial Key Research and Development Program (BE2020114).

Reference

[1] I.K. Mishra, H. Zhou, J. Sun, F. Qin, K. Dahal, J. Bao, S. Chen, Z. Ren, Hierarchical CoP/Ni_5P_4/CoP microsheet arrays as a robust pH-universal electrocatalyst for efficient hydrogen generation, Energy Environ. Sci. 11 (8) (2018) 2246-2252.

[2] N. Armaroli, V. Balzani, The future of energy supply: Challenges and opportunities, Angew. Chem., Int. Ed. 46 (1-2) (2007) 52-66.

[3] H. Zhou, F. Yu, J. Sun, R. He, S. Chen, C.W. Chu, Z. Ren, Highly active catalyst derived from a 3D foam of $Fe(PO_3)_2$/Ni_2P for extremely efficient water oxidation, Proc. Natl. Acad. Sci. U. S. A 114 (22) (2017) 5607-5611.

[4] I. Roger, M.A. Shipman, M.D. Symes, Earth-abundant catalysts for electrochemical and photoelectrochemical water splitting, Nat. Rev. Chem. 1 (1) (2017).

[5] K. Gao, O.A. Sahraei, M.C. Iliuta, Development of residue coal fly ash supported nickel catalyst for H2 production via glycerol steam reforming, Appl. Catal., B 291 (2021).

[6] C. Rocha, M.A. Soria, L.M. Madeira, Olive mill wastewater valorization through

steam reforming using hybrid multifunctional reactors for high-purity H_2 production, Chem. Eng. J 430 (2022) 132651.

[7] Z. Dai, H. Geng, J. Wang, Y. Luo, B. Li, Y. Zong, J. Yang, Y. Guo, Y. Zheng, X. Wang, Q. Yan, Hexagonal-Phase Cobalt Monophosphosulfide for Highly Efficient Overall Water Splitting, ACS Nano 11 (11) (2017) 11031-11040.

[8] K. Liu, H. Zhong, F. Meng, X. Zhang, J. Yan, Q. Jiang, Recent advances in metal–nitrogen–carbon catalysts for electrochemical water splitting, Mater. Chem. Front. 1 (11) (2017) 2155-2173.

[9] Z. Cheng, Y. Xiao, W. Wu, X. Zhang, Q. Fu, Y. Zhao, L. Qu, All-pH-Tolerant In-Plane Heterostructures for Efficient Hydrogen Evolution Reaction, ACS Nano 15(7) (2021) 11417-11427.

[10] M. Yao, B. Wang, B. Sun, L. Luo, Y. Chen, J. Wang, N. Wang, S. Komarneni, X. Niu, W. Hu, Rational design of self-supported Cu@WC core-shell mesoporous nanowires for pH-universal hydrogen evolution reaction, Appl. Catal., B 280 (2021) 119451.

[11] Q. Wang, R. Guo, Z. Wang, D. Shen, R. Yu, K. Luo, C. Wu, S. Gu, Progress in carbon-based electrocatalyst derived from biomass for the hydrogen evolution reaction, Fuel 293 (2021) 120440.

[12] L.-H. Xu, H.-B. Zeng, X.-J. Zhang, S. Cosnier, R.S. Marks, D. Shan, Highly active $M_2P_2O_7$@NC (M = Co and Zn) for bifunctional electrocatalysts for ORR and HER, J. Catal. 377 (2019) 20-27.

[13] L. Feng, S. Li, D. He, L. Cao, G. Li, P. Guo, J. Huang, Heterostructured VN/Mo_2C

Nanoparticles as Highly Efficient pH-Universal Electrocatalysts toward the Hydrogen Evolution Reaction, ACS Sustainable Chem. Eng. 9 (45) (2021) 15202-15211.

[14] J. Jiang, R. Sun, X. Huang, H. Cong, J. Tang, W. Xu, M. Li, Y. Chen, Y. Wang, S. Han, H. Lin, CoS_2 quantum dots modified by ZIF-67 and anchored on reduced graphene oxide as an efficient catalyst for hydrogen evolution reaction, Chem. Eng. J 430 (2022) 132634.

[15] G. Zhou, M. Li, Y. Li, H. Dong, D. Sun, X. Liu, L. Xu, Z. Tian, Y. Tang, Regulating the Electronic Structure of CoP Nanosheets by O Incorporation for High- Efficiency Electrochemical Overall Water Splitting, Adv. Funct. Mater. 30 (7) (2019) 1905252.

[16] J. Tian, Q. Liu, A.M. Asiri, X. Sun, Self-supported nanoporous cobalt phosphide nanowire arrays: an efficient 3D hydrogen-evolving cathode over the wide range of pH 0-14, J. Am. Chem. Soc. 136(21) (2014) 7587-7590.

[17] T. Liu, P. Li, N. Yao, G. Cheng, S. Chen, W. Luo, Y. Yin, CoP-Doped MOF-Based Electrocatalyst for pH-Universal Hydrogen Evolution Reaction, Angew. Chem., Int. Ed. 58 (14) (2019) 4679-4684.

[18] C. Guan, W. Xiao, H. Wu, X. Liu, W. Zang, H. Zhang, J. Ding, Y.P. Feng, S.J. Pennycook, J. Wang, Hollow Mo-doped CoP nanoarrays for efficient overall water splitting, Nano Energy 48 (2018) 73-80.

[19] J. Zhu, L. Hu, P. Zhao, L.Y.S. Lee, K.Y. Wong, Recent Advances in Electrocatalytic Hydrogen Evolution Using Nanoparticles, Chem. Rev. 120 (2) (2020) 851-918.

[20] W. Li, J. Liu, P. Guo, H. Li, B. Fei, Y. Guo, H. Pan, D. Sun, F. Fang, R. Wu, Co/CoP Heterojunction on Hierarchically Ordered Porous Carbon as a Highly Efficient

Electrocatalyst for Hydrogen and Oxygen Evolution, Adv. Energy Mater. 11 (42) (2021) 2102134.

[21] Q. Liu, J. Tian, W. Cui, P. Jiang, N. Cheng, A.M. Asiri, X. Sun, Carbon nanotubes decorated with CoP nanocrystals: a highly active non-noble-metal nanohybrid electrocatalyst for hydrogen evolution, Angew. Chem., Int. Ed. 53 (26) (2014) 6710-6714.

[22] X. Huang, X. Xu, C. Li, D. Wu, D. Cheng, D. Cao, Vertical CoP Nanoarray Wrapped by N,P- Doped Carbon for Hydrogen Evolution Reaction in Both Acidic and Alkaline Conditions, Adv. Energy Mater. 9 (22) (2019) 1803970.

[23] E. Vijayakumar, S. Ramakrishnan, C. Sathiskumar, D.J. Yoo, J. Balamurugan, H.S. Noh, D. Kwon, Y.H. Kim, H. Lee, MOF-derived CoP-nitrogen-doped carbon@NiFeP nanoflakes as an efficient and durable electrocatalyst with multiple catalytically active sites for OER, HER, ORR and rechargeable zinc-air batteries, Chem. Eng. J 428 (2022) 131115.

[24] J.N. Tiwari, N.K. Dang, S. Sultan, P. Thangavel, H.Y. Jeong, K.S. Kim, Multi-heteroatom-doped carbon from waste-yeast biomass for sustained water splitting, Nat. Sustain. 3 (7) (2020) 556-563.

[25] K. An, X. Xu, X. Liu, Mo2C-Based Electrocatalyst with Biomass-Derived Sulfur and Nitrogen Co-Doped Carbon as a Matrix for Hydrogen Evolution and Organic Pollutant Removal, ACS Sustainable Chem. Eng. 6 (1) (2017) 1446-1455.

[26] S. Gao, X. Li, L. Li, X. Wei, A versatile biomass derived carbon material for oxygen reduction reaction, supercapacitors and oil/water separation, Nano Energy 33

(2017) 334-342.

[27] N. Prabu, R.S.A. Saravanan, T. Kesavan, G. Maduraiveeran, M. Sasidharan, An efficient palm waste derived hierarchical porous carbon for electrocatalytic hydrogen evolution reaction, Carbon 152 (2019) 188-197.

[28] X. Wang, J. Du, Q. Zhang, L. Gu, L. Cao, H.-P. Liang, In situ synthesis of sustainable highly efficient single iron atoms anchored on nitrogen doped carbon derived from renewable biomass, Carbon 157 (2020) 614-621.

[29] X. Li, B.Y. Guan, S. Gao, X.W. Lou, A general dual-templating approach to biomass-derived hierarchically porous heteroatom-doped carbon materials for enhanced electrocatalytic oxygen reduction, Energy Environ. Sci. 12 (2) (2019) 648-655.

[30] C. Hu, H. Jin, B. Liu, L. Liang, Z. Wang, D. Chen, D. He, S. Mu, Propagating Fe-N4 active sites with Vitamin C to efficiently drive oxygen electrocatalysis, Nano Energy 82 (2021) 105714.

[31] S. Chen, S. Wang, P. Hao, M. Li, Y. Zhang, J. Guo, W. Ding, M. Liu, J. Wang, X. Guo, N,O-C Nanocage-mediated high-efficient hydrogen evolution reaction on IrNi@N,O-C electrocatalyst, Appl. Catal., B 304 (2022) 120996.

[32] Y. Zhou, Y. Leng, W. Zhou, J. Huang, M. Zhao, J. Zhan, C. Feng, Z. Tang, S. Chen, H. Liu, Sulfur and nitrogen self-doped carbon nanosheets derived from peanut root nodules as high-efficiency non-metal electrocatalyst for hydrogen evolution reaction, Nano Energy 16 (2015) 357-366.

[33] L. Yang, R. Liu, L. Jiao, Electronic Redistribution: Construction and Modulation

of Interface Engineering on CoP for Enhancing Overall Water Splitting, Adv. Funct. Mater. 30 (14) (2020).

[34] S. Mao, C. Wang, Y. Wang, The chemical nature of N doping on N doped carbon supported noble metal catalysts, J. Catal. 375 (2019) 456-465.

[35] S. Yang, Y. Wang, H. Zhang, Y. Zhang, L. Liu, L. Fang, X. Yang, X. Gu, Y. Wang, Unique three-dimensional $Mo_2C@MoS_2$ heterojunction nanostructure with S vacancies as outstanding all-pH range electrocatalyst for hydrogen evolution, J. Catal. 371 (2019) 20-26.

[36] Y. Pan, K. Sun, Y. Lin, X. Cao, Y. Cheng, S. Liu, L. Zeng, W.-C. Cheong, D. Zhao, K. Wu, Z. Liu, Y. Liu, D. Wang, Q. Peng, C. Chen, Y. Li, Electronic structure and d-band center control engineering over M-doped CoP (M = Ni, Mn, Fe) hollow polyhedron frames for boosting hydrogen production, Nano Energy 56 (2019) 411-419.

[37] C.Y. Su, L.C. Wang, W.S. Liu, C.C. Wang, T.P. Perng, Photocatalysis and Hydrogen Evolution of Al- and Zn-Doped TiO2 Nanotubes Fabricated by Atomic Layer Deposition, ACS Appl. Mater. Interfaces 10 (39) (2018) 33287-33295.

[38] H. Yan, Y. Xie, A. Wu, Z. Cai, L. Wang, C. Tian, X. Zhang, H. Fu, Anion-Modulated HER and OER Activities of 3D Ni-V-Based Interstitial Compound Heterojunctions for High-Efficiency and Stable Overall Water Splitting, Adv. Mater. 31 (23) (2019) e1901174.

[39] Y. Zheng, Y. Jiao, M. Jaroniec, S.Z. Qiao, Advancing the electrochemistry of the hydrogen-evolution reaction through combining experiment and theory, Angew. Chem., Int. Ed. 54 (1) (2015) 52-65.

[40] T. Shinagawa, A.T. Garcia-Esparza, K. Takanabe, Insight on Tafel slopes from a microkinetic analysis of aqueous electrocatalysis for energy conversion, Sci Rep 5 (2015) 13801.

[41] Z. Chen, R. Wu, Y. Liu, Y. Ha, Y. Guo, D. Sun, M. Liu, F. Fang, Ultrafine Co Nanoparticles Encapsulated in Carbon-Nanotubes-Grafted Graphene Sheets as Advanced Electrocatalysts for the Hydrogen Evolution Reaction, Adv. Mater. 30 (30) (2018) e1802011.